Lithosphere

Research Article

Activity Analysis of the Fuyu North Fault, China: Evidence from the Time-Series InSAR, GNSS, Seismic Reflection Profile, and Plate Dynamics

Bin Liu [ID],[1] **Qigang Jiang** [ID],[1] **Ziwen Zhang** [ID],[2] **Yuanhua Li** [ID],[1] **Mengyao Shi** [ID],[3] **Zhenchao Zhang** [ID],[1] **Pengfei Shi** [ID],[1] **Huaxin Liu** [ID],[1] **Sen Zhang** [ID],[1] and **Peng Wang** [ID][1]

[1]*College of Geo-Exploration Science and Technology, Jilin University, Changchun 130026, China*
[2]*School of Aviation Engineering, Guangzhou Maritime University, Guangzhou 510725, China*
[3]*School of Land Science and Technology, China University of Geosciences, Beijing 100083, China*

Correspondence should be addressed to Qigang Jiang; jiangqigang@jlu.edu.cn

Earthquake disasters are frequent, and the seismic intensity is large in Northeast China. Earthquake activity research is an important aspect of earthquake disaster management. We chose some unconventional means to study fault activity, to find updated activity evidence. The Ms 5.3 earthquake occurred near the Fuyu North Fault (FNF) of China on May 27, 2018. Using the Sentinel-1B descending orbit data from 2016 to 2019, the line-of-sight (LOS) surface deformation in the study area was calculated by using the small baseline subset (SBAS) method. After transforming to the horizontal EW deformation, the variance component estimation method was used for fusion reconstruction with the EW data of the surrounding GNSS stations. The polynomial least square method is used to fit the fault slip rate of three EW data on the surface trace of the FNF. The fitting results of the three regions show that the horizontal eastward distribution rate of the upper plate is significantly greater than that of the lower plate, which is left-lateral clockwise torsion. The vertical structural deformation caused by the growth strata of the upper and lower plates of the upper SYT2 seismic profile of the FNF is quantitatively calculated, and the thrust rate of the upper plate is 0.2 mm/y relative to that of the lower plate. Based on the Li Siguang chessboard structure model, we found that the compression stress in the north-south direction is gradually weakened, and the compression stress in the east-west direction is gradually enhanced. Through the Coulomb stress analysis, the three events of CMT only induced the historical focal location of the surrounding part. The events of 2017 did not induce the events of 2018, but the events of 2019 were related to the induced effects of 2017 and 2018.

1. Introduction

Active faults have, in SSR-1 [1], released by the International Atomic Energy Agency, a clear definition: (a) faults that show past movements or repeated movements (major surface deformation and/or dislocation) in a reasonable period to infer that further movements may occur on or near the surface. In highly active areas, seismic and geological data are consistent and/or only show shorter intervals of earthquake recurrence, and tens of thousands of years or so of cycles may be appropriate to assess capable faults. It may take longer in less active areas. (b) The structural relationship with known faults has been demonstrated, one of which may lead to another movement on or near the surface. (c) The maximum potential earthquake related to the original earthquake structure is large enough and deep enough that it can be reasonably inferred that in the geodynamic environment of the site, movement may occur on the surface or near the surface (SSR-1, p. 18). If any of these is satisfied, a fault can be confirmed as an active fracture. Earthquakes can lead to surface rupture, and even buried faults may also lead to surface deformation of sediments [2, 3]. These can threaten facilities and human life. The Fuyu North Fault (FNF) is an important east-west concealed active fault in

the Songliao Basin (SB), China, and it easily accumulates energy in the structure that can lead to earthquakes [4–9]. This region is currently known as the site of one of the strongest earthquakes in Northeast China. Quaternary sediments with a certain thickness have been found on the surface of the FNF, and no obvious earthquake surface rupture has been found following many earthquakes. In recent years, many studies have involved the relationship between Quaternary thickness and seismic surface rupture or fault surface rupture [10–12]. Although Quaternary sediments can buffer and absorb displacement and surface microgeomorphology may be more or less affected, farmland leveling can only transfer and mitigate vertical and horizontal displacement of the surface; it cannot eliminate this displacement [13].

In the past, the active detection of concealed faults was mainly determined by trenching and other methods to expose stratigraphic dislocation [14–17], on-site investigation of seismic traces such as fault scarps [18–23], gully dislocation [24–27], sand gushing and sand liquefaction [28–31], and stress analysis modeling of geological rock mass [32–37]. However, in recent years, a large number of seismic reflection profiles have accumulated near the FNF [38], which can be used to reveal the vertical deformation of the growing strata. The "flower" structures are the most typical sign of strike-slip faults in the seismic reflection profile [39]. Therefore, the strike-slip characteristics of the FNF need to be further verified. Interferometric Synthetic Radar (InSAR) and GNSS are newly emerging remote sensing monitoring methods. InSAR can monitor large-scale surface displacement with a high spatial resolution and centimeter-to-millimeter accuracy [40–45], which has the advantages of providing large imaging data and a wide distribution area. However, InSAR measurements are one-dimensional measurements along the radar line of sight (LOS) [46, 47]. Although GNSS can accurately measure three-dimensional (3D) surface displacement, its expensive construction cost hinders its rapid development. The spatial resolution of GNSS monitoring results cannot be compared with that of InSAR. To solve this problem, the existing research generally performs spatial interpolation on GNSS data, to obtain the 3D deformation field with the same spatial resolution of InSAR. It is clear, however, that GNSS interpolation results depend on the density and distribution of its stations and cannot reflect local deformation information. For the study area, where GNSS and InSAR data can be obtained simultaneously, their complementary advantages in monitoring dimensions and spatial resolution can be fully utilized. The fusion of GNSS and InSAR data to reconstruct 3D surface deformations can solve the rank deficiency and morbid problem of the InSAR 3D deformation estimation function model [48]. The first design for polynomial regression experiments appeared in Gergonne's paper in 1815 [49, 50]. The polynomial regression model is widely used in data smoothing and data interpolation.

We can use the reconstructed 3D deformation data to extract the data near the FNF for polynomial least square fitting, to find evidence of horizontal sliding activity of the FNF. It is hoped that the activity and sliding condition of the FNF will be able to be analyzed from previous plate dynamics research results, and a regional tectonic model of the study area will be established with the use of new and less commonly utilized methods. This is the aim of this work.

2. Seismo-Geological Background

2.1. Tectonic Characteristics. Although there is a lack of deep and large faults near the FNF, the tectonic scale is small, the movement is weak, and the focal depth is shallow; the FNF is located at the intersection of the central depression belt and the southeast uplift belt of the SB (Figure 1). There are two conjugate structures in the northeast and northwest, which are prone to generating energy accumulation and earthquakes. The FNF began in the late Permian due to the collision between the Jiameng block and the North China plate; its formation time was earlier than the NE and NW faults [51, 52]. The FNF is 26 km long and nearly east-west trending. It extends eastward from Sunjia Town to Dawa Town, which is the northern boundary of the Fuyu Uplift, with a fault strike of approximately 60°–80°. The SB is a composite sedimentary basin with a Cenozoic faulted-sag dual structure, developed on the basement of Inner Mongolia and the fold of the Jihei trough in the late Hercynian period [53, 54]. Since the Middle Jurassic, the SB has experienced the closure of ancient Asia, the closure of the Mongolia Okhot subocean, and the subduction of the ancient Pacific Plate, which is known to have continued into the Late Cretaceous [55, 56]. Plate tectonic interactions led to mantle upwelling and produced fault structures and volcanic activities in the basin [57, 58]. In the early stage, under the influence of the extensional stress of the Eurasian Plate and Pacific Plate, multiple faulted-sag structures, such as Wangfu, Dehui, and Lishu, developed in the southern SB (Figure 1). The depression structure in the SB is a new structure dominated by stable subsidence. At the end of structural deposition in the depression, the hanging wall of the FNF was reversed and uplifted by the southeast uplift area under the action of the east-west compressive stress, and the new tectonic movement was characterized by thrust nappe. The tectonic evolution stages of the SB are the uplift period, faulted-sag period, depression period, atrophy period, and uplift period, and the superposition basin of the faulted sag and depression was formed.

2.2. Seismic Activity Characteristics. The spatial distribution of moderate and strong earthquakes in the Songyuan area, where the FNF is located, is uneven, and there are more earthquakes in the south-central area. The distribution of the earthquake distribution map in Northeast China from 1905 to 2022 in depth, time, and magnitude is shown in Figure 2. The spatial activity of small earthquakes is also unevenly distributed. The frequency of small earthquakes is higher in places where moderate and strong earthquakes occur. The small earthquake activity near Songyuan is significantly enhanced. Earthquakes occur more intensively in Ningjiang District and in the Dawa and Fenghua area of Songyuan and distribute along the NE-trending FNF and NW-trending Second Songhua River Fault and its intersection. There was a strong earthquake with Ms = 6.75 before
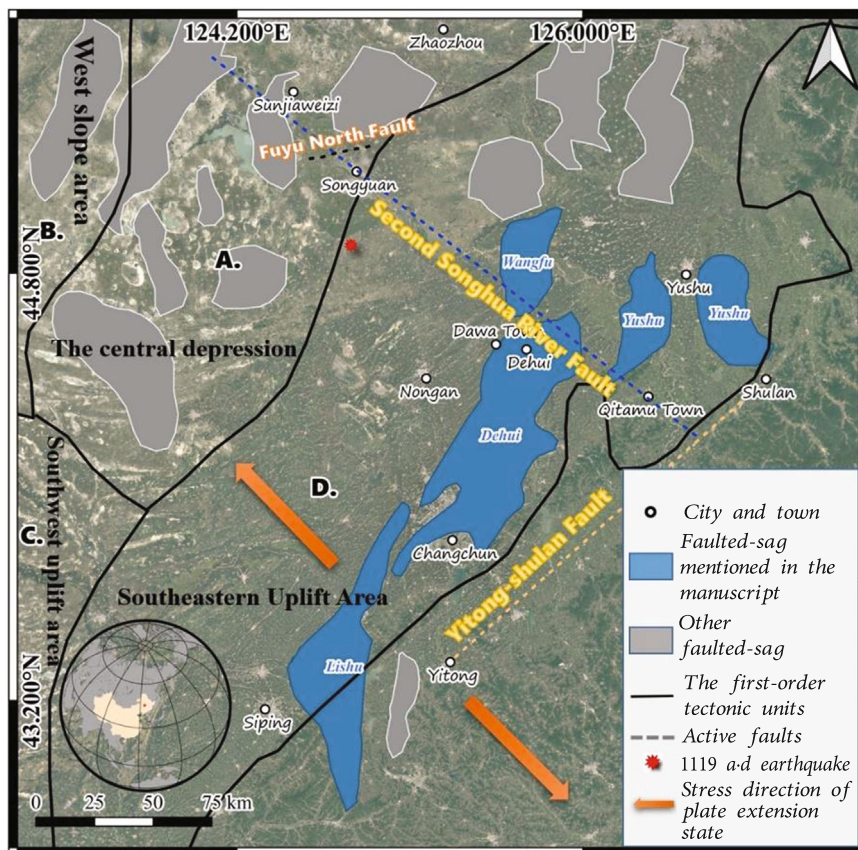
FIGURE 1: Distribution map of faulted-sag groups around the FNF (modified by Zhao et al. [59]). There are six primary tectonic zones in the SB, and the two zones that are not identified are the north descent area and northeast uplift area. The orange arrow shows that the SB formed faulted-sag groups under the extension of the Pacific Plate and the Eurasian Plate during the faulted-sag period.

A.D. 1119, which was related to the NE-trending fault in the tectonic part of the city; this historical earthquake had the greatest impact on Songyuan. Since 2003, the earthquakes in the Songyuan area have generally shown an accelerated energy release trend, and multiple swarm activities have occurred. In 2003, 2006, 2010, and especially 2017–2019, earthquakes with Ms 4.9, Ms 5.2, and Ms 5.0 occurred near the FNF for three consecutive years, and the occurrence positions were similar. From 2020 to now, the earthquakes have weakened obviously.

2.3. Stress Field and Focal Mechanism Solution. Sheng et al. [38, 60] drew a map of the principal compressive stress and tensile stress in the Songyuan area (Figure 3(a)) based on 1755 P-wave initial motion data of 659 earthquakes in the Jilin network of China. They collected the focal mechanism data of the Songyuan area and drew a comprehensive focal mechanism map of the Songyuan area (Figure 3(b)). From the two maps, it can be seen that the main compressive stress in the Songyuan area points to the northwest as a whole and is in the near EW horizontal compressive stress environment. The strike of the focal mechanism is mainly northeast and northwest, and the rupture mode of earthquakes is mainly thrust. The rupture of individual earth-

quakes in the east has normal faults and strike-slip properties.

3. Polynomial Least Square Fitting

To obtain the surface deformation of the FNF, we selected a Sentinel-1B image provided by the European Space Agency (ESA). Only 87 Sentinel-1B constituted the full time-series data from 2016 to 2019. The digital elevation model (DEM) data in the study area were generated by the ALOS DSM data, with a resolution of 30 m, and provided by the Japan Aerospace Exploration Agency. In addition, precise orbit data (POD) for Sentinel-1B were provided by the ESA. We used GACOS data to correct the atmospheric delay error [61, 62]. Details of the image are shown in Table 1. To increase the number and reliability of selected time-series coherence (TC) points, we first calculated and analyzed the average spatial coherence of the interferograms and then constructed an inversion network with high coherence interferograms. As shown in Figure 4(a), the interference pairs in the crop growth period from April to September each year are lowly coherent, and the interference pairs in winter are highly coherent. Affected by farmland, the average spatial coherence (SC) of the whole study area is about
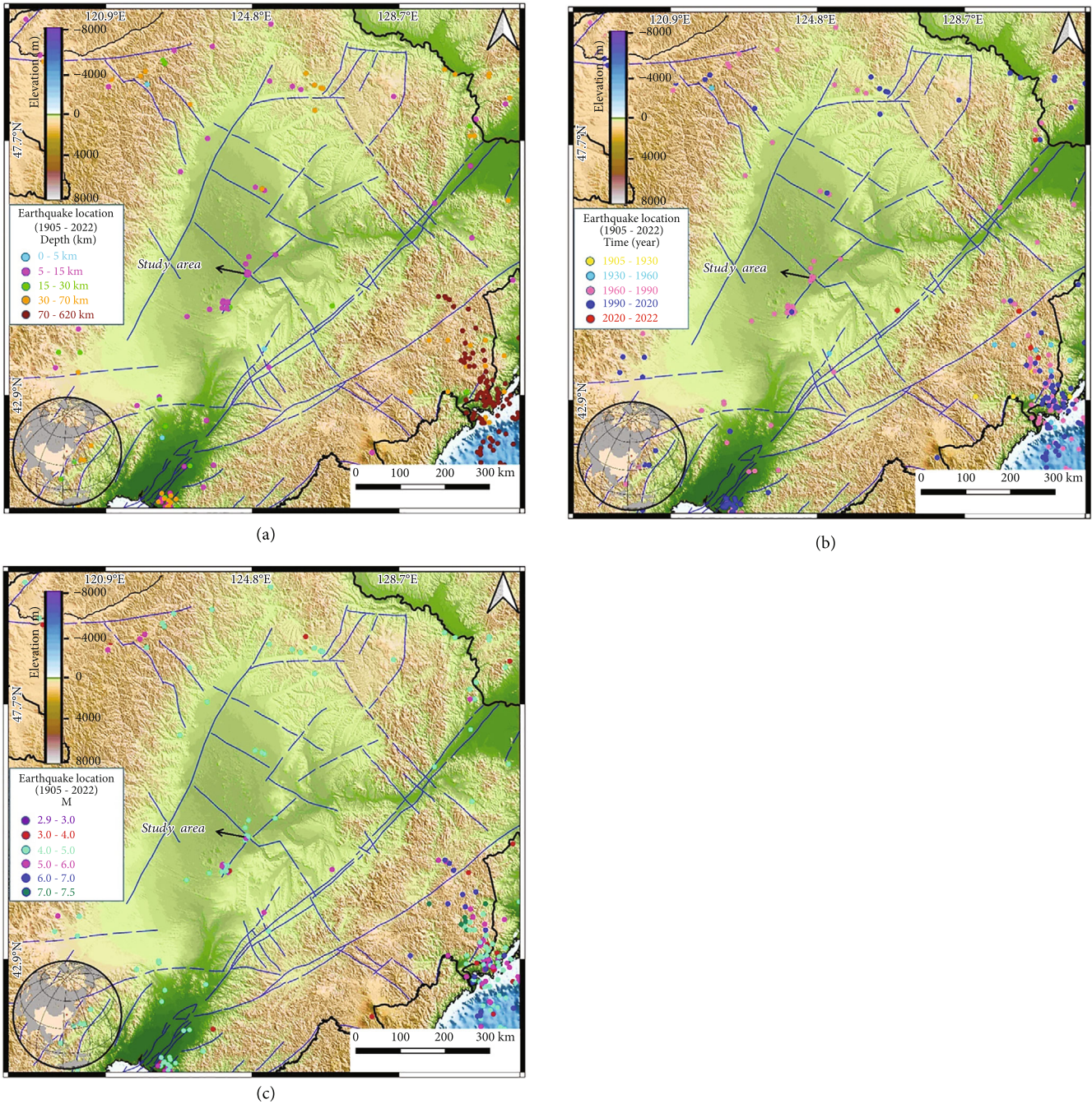
(a)

(b)

(c)

FIGURE 2: (a) The distribution of seismic location in depth can be seen that the seismic depth in the Songnen Plain is 5–15 km, and the seismic depth in the lower right corner is 70–620 km, which may be related to the subduction of the Pacific Plate. (b) Time distribution of earthquake location. (c) The distribution of earthquake location on magnitude. The Songnen Plain is mainly distributed with 4-5 earthquakes.

0.4, so the vertical spatial baseline threshold range was set to 200 m, and the time baseline threshold was set to 12–48 days. The annual settlement calculated by SBAS is shown in Figure 4(b). The location of the InSAR image is shown in Figures 4(c) and 4(d). As shown in Figure 4(e), the motion direction and size of the ground target in the west direction are constrained by the projection of SAR image descending orbit and ascending orbit in the east-west direc-

tion. Unfortunately, there is only ESA Sentinel-1B descending orbit data in this study area. In order to compensate for the only InSAR data, we referred to Hu et al.'s variance component estimation (VCE) method [48] and used the 2018 GNSS east-west data to constrain the InSAR data to obtain a high-precision 3D deformation field in the east-west direction (Figure 5). The variance component estimation method is shown in equations (1)–(7).
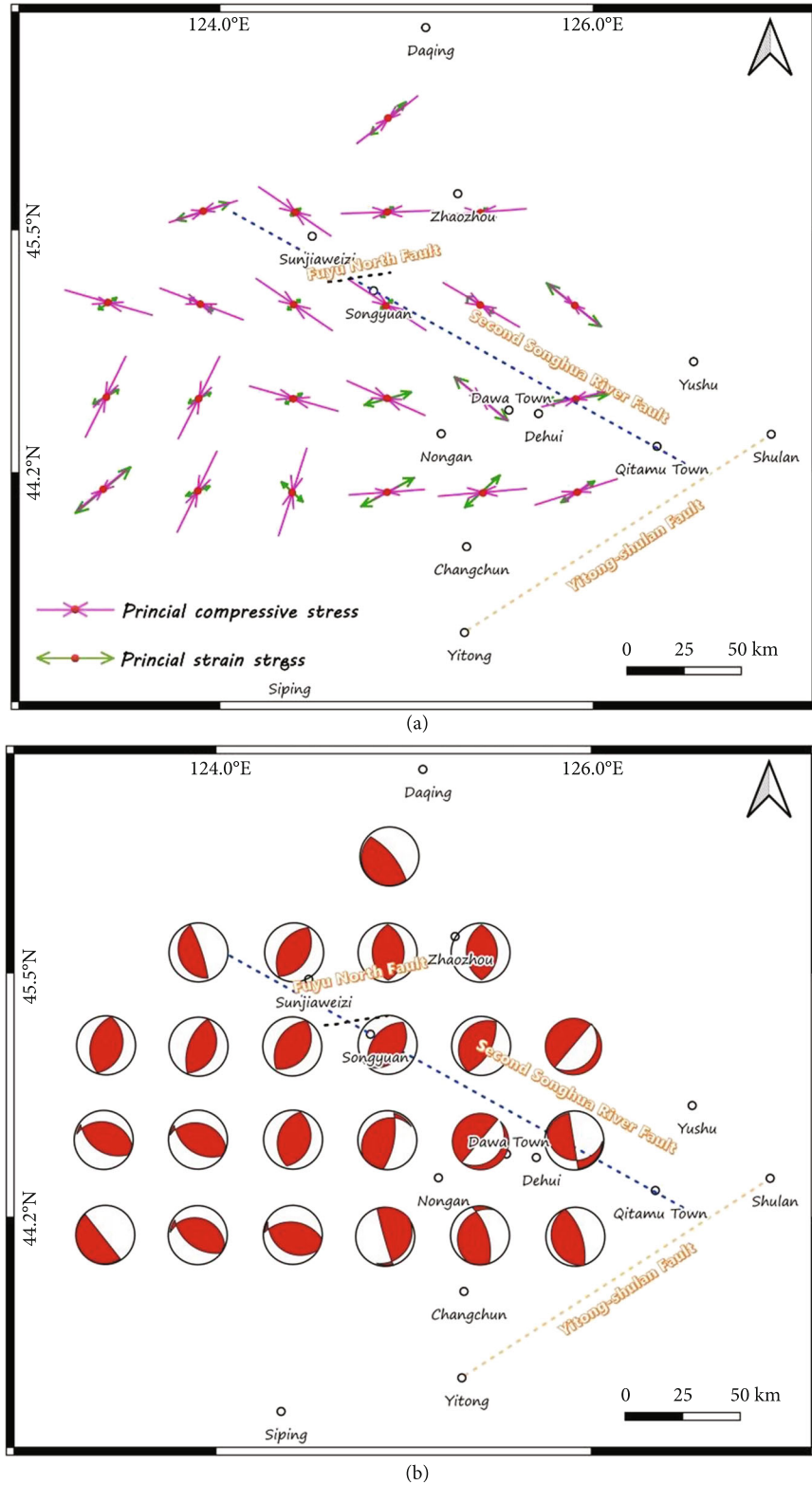
Figure 3: (a) The distribution maps of principal compressive stress and assertive stress in the Songyuan area. (b) The comprehensive focal mechanism in the Songyuan area (modified by Sheng et al. [38, 60]).

As shown in Figure 4(e), the moving direction and size of the east-west ground target were constrained by the projection of the ascending and descending orbit SAR image in the east-west direction. To make up for the fact that only the InSAR descending data were available, we used the 2018 GNSS and InSAR data fusion method to obtain the high-

TABLE 1: The SAR dataset information.

Satellite	Time span	Image number	Incidence angle (°)	Heading angle (°)	Resolution (Rg × Azim)	Number of interferograms
Sentinel-1B (IWS)	20161007 20191231	87	43.7737°	-170.6575972	2.33 × 13.94	156

precision 3D deformation field in the east-west direction (Figure 5).

We assumed that a SAR image in the study area constitutes b interference pairs. For a coherent point m in the nth interference pair, assuming that point m has uniform deformation, we have

$$\text{Disp}_{\text{los}}^{nm} = [t_n \bullet B_e^{nm}] \bullet [v_e^m]^T. \tag{1}$$

In the equation, v_e^m is the east-west deformation rate of coherent point m. $\text{Disp}_{\text{los}}^{nm}$ is the LOS variable of the coherent point m on the nth interference pair. t_n is the time interval of the nth interference pair. B_e^{nm} is an east-west projection vector on the coherent point m in the LOS direction, such that

$$B_e^m = -\sin\theta_{\text{inc}}^m \sin\left(\alpha_{\text{azi}}^m - \frac{3\pi}{2}\right). \tag{2}$$

In the equation, θ_{inc}^m is the incident angle of coherent point m in the SAR image, and α_{azi}^m is the heading angle of coherent point m in the SAR image. We selected the east-west data of GNSS stations around the FNF in 2018 and InSAR to obtain the LOS deformation results using SBAS and converted the east-west data. They all used Kriging interpolation to raster data with a resolution of 275 m.

$$[G_e^{nm}] = t_n \bullet [v_e^m]^T. \tag{3}$$

In the equation, G_e^{nm} denotes the type of variable of coherent point n in the east-west direction obtained by interpolation of GNSS measurements. Through the least square model, the interpolated GNSS and InSAR data can be fused to solve the 3D surface deformation.

$$O = AX + V. \tag{4}$$

In the equation, $X = [v_e^m]^T$ is the east-west deformation rate to be calculated. $O = [\text{Disp}_{\text{los}}^{1m} \cdots \text{Disp}_{\text{los}}^{nm} G_e^{1m} \cdots G_e^{1m}]^T$ is the observation value composed of m InSAR east-west interpolation measurements and m GNSS east-west interpolation. V is the corresponding observation residual. A is the design matrix.

$$A = [t_1 \bullet B_e^{1m} \cdots t_n \bullet B_e^{nm} \ t_1 \cdots t_n]^T. \tag{5}$$

By using the least square adjustment and VCE method to calculate ρ^2 in P, the optimal estimation of the 3D surface deformation rate can be obtained:

$$\hat{X} = (B^T P B)^{-1} B^T P O. \tag{6}$$

In the equation, P is the weight matrix of variance of each observation.

$$P = \text{diag}\left(\frac{1}{\rho_{\text{Disp}_{\text{los}}^{1m}}^2} \cdots \frac{1}{\rho_{\text{Disp}_{\text{los}}^{nm}}^2} \frac{1}{\rho_{G_e^{1m}}^2} \cdots \frac{1}{\rho_{G_e^{nm}}^2}\right). \tag{7}$$

The process of VCE can be simply described as follows. Firstly, the initial weights of all kinds of observations are determined, and the least square method is used for preadjustment. Then, according to certain principles, the variance of the observation is iteratively estimated by using the observed value correction obtained from the adjustment, until the error in the unit weight of all kinds of observations is equal.

The reconstructed data were fused by the VCE method, as shown in Figure 5. Global CMT only provided seismic parameters of three events in 2017, 2018, and 2019 (Table 2). The focal mechanism solution shows that the earthquake was a strike-slip. Table 3 collects the historical seismic parameters of Figure 5. In addition to the three events in Table 2, the rest were obtained from the China Seismic Network, but this only provided the focal depth and magnitude.

As shown in Figure 5, we selected points in three regions for polynomial least square fitting. After many experiments, we selected the values of R^2 and RMSE with a polynomial of 7th power as the optimal values. The polynomial equation is [49]

$$V = p_1 \times x^7 + p_2 \times x^6 + p_3 \times x^5 + p_4 \times x^4 \\ + p_5 \times x^3 + p_6 \times x^2 + p_7 \times x + p_8, \tag{8}$$

where V represents the velocity component of the station parallel to the fault strike and p is the polynomial parameter. According to equation (8), we, respectively, fitted the fault sliding rate of the three regional points of the FNF in Figure 5. The FNF is located at $x = 0$ km, and $x > 0$ was set as the upper plate of the FNF; otherwise, it was the lower plate of the FNF. The results are shown in Table 4, and the fitted curve is the fitted value of the inversion convergence rate. The values of the fitting curves of the upper plate in the three regions are all greater than those of

(a)
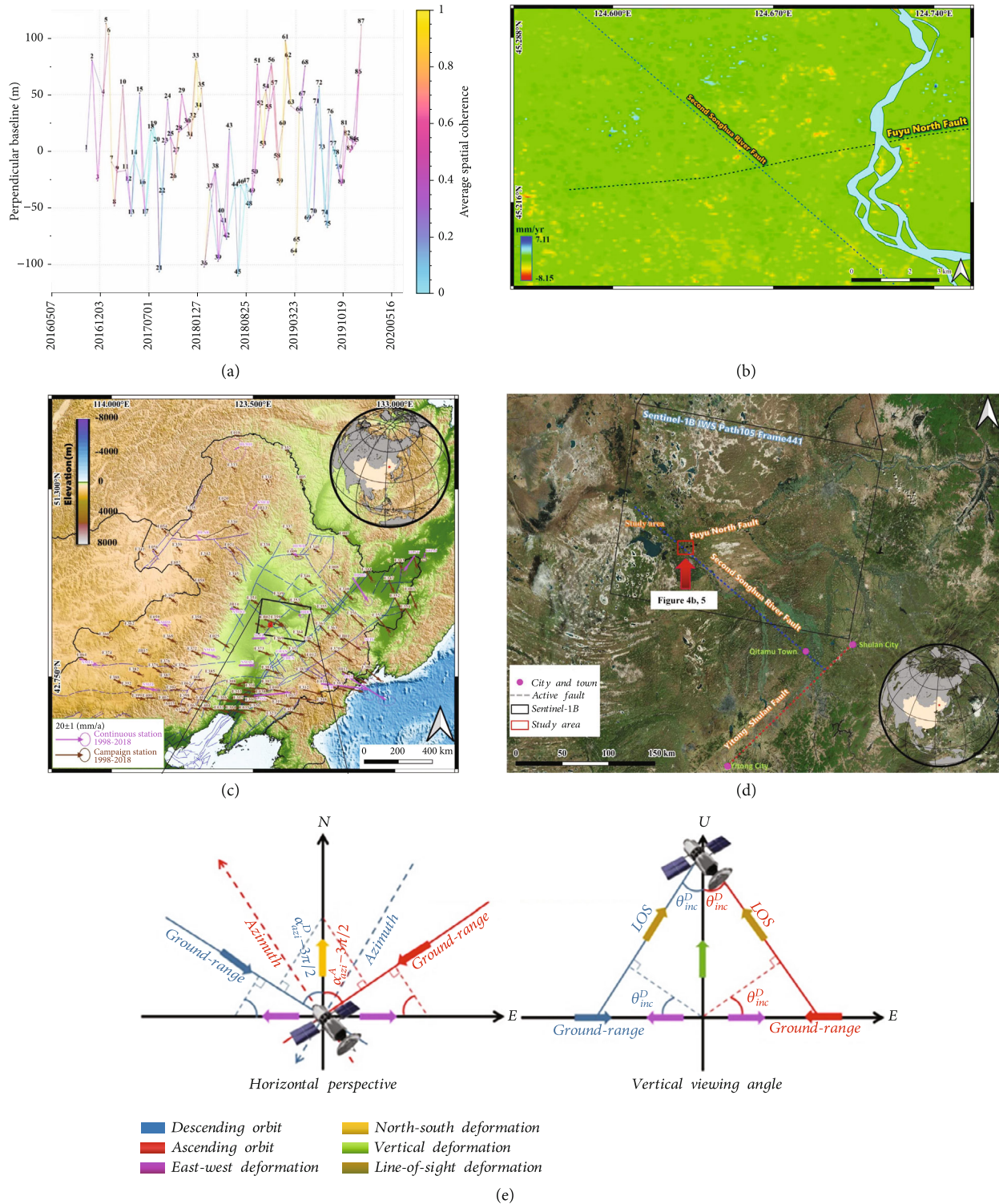

(b)

(c)

(d)

(e)

FIGURE 4: (a) The time-space baseline map of interferometry combinations in SBAS-InSAR from 2016 to 2019. The color values of the connection lines represent the average spatial coherences of the interferometry. (b) The LOS annual subsidence results of Sentinel-1B data in the study area from 2016 to 2019 are based on the SBAS method. (c) The velocity field distribution map of the 1998–2018 GNSS campaign and continuous stations in northeast China and (d) Sentinel-1B IWS and the location of the study area. (e) Geometric relationship of descending and ascending orbit SAR image imaging.

the lower plate, and they are all positive, indicating that the upper plate and the lower plate of the FNF move eastward horizontally, and the horizontal eastward movement

rate of the lower plate is less than that of the upper plate. Therefore, the lower plate of the FNF has left-handed torsion relative to the upper plate. Table 2 shows that
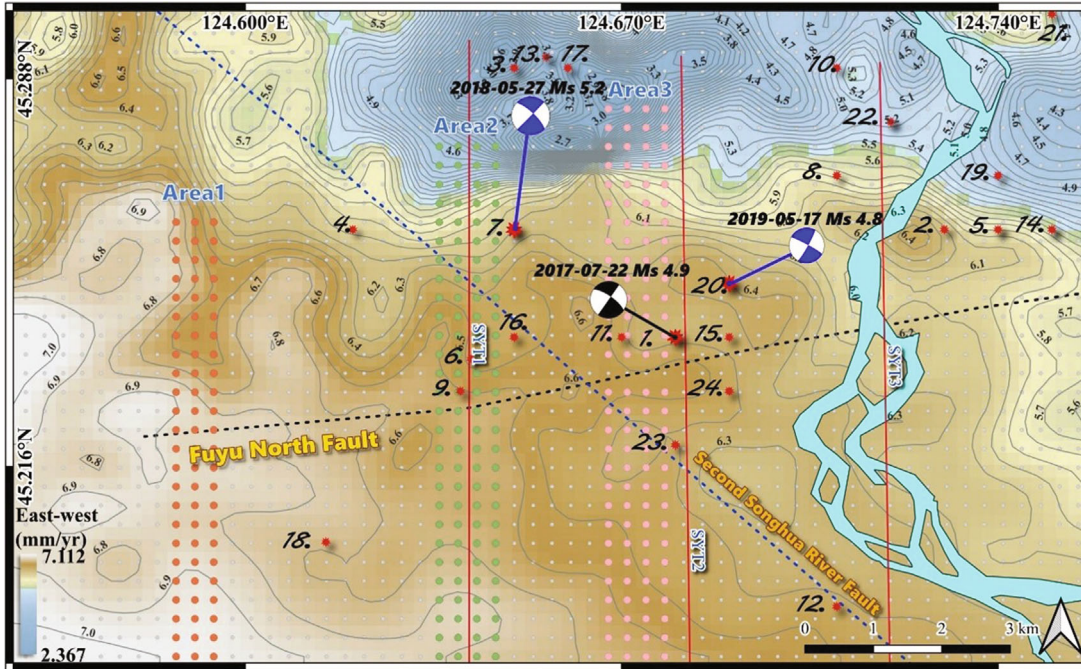
FIGURE 5: The 2018 GNSS east-west data and the InSAR east-west annual subsidence data are based on the VCE method to obtain grid data with a resolution of 275 m (unit: east-west mm/yr). The contour interval was 0.1 mm/yr. The points in the Area1, Area2, and Area3 regions were used to fit the fault slip velocity. The parameters of the three source spheres are shown in Table 2. The seismic reflection profiles of SYT1, SYT2, and SYT3 are shown in Section 4. The red polygon is the source location of historical earthquakes, and the number size is arranged in the order of earthquakes. Light blue is the Second Songhua River.

TABLE 2: Global CMT catalog for Songyuan, China.

Date	Lon (°)	Lat (°)	Depth (km)	Ms	Fault plane	Strike (°)	Dip (°)	Slip (°)	Source sphere
22 July 2017	124.69	45.25	12.1	4.9	1	305	73	0	
					2	35	90	−163	
27 May 2018	124.65	45.26	14.2	5.2	1	314	75	−1	
					2	44	89	−165	
17 May 2019	124.68	45.24	14.2	5.0	1	29	84	−175	
					2	299	85	−6	

the location of the three earthquakes was close and the focal depth concentrated at 12–14.2 km, indicating that the locking depth of the FNF fault is not more than 14.2 km.

4. Seismic Reflection Profile

The FNF area has a dualistic structure consisting of faulted sag. In the late sedimentary period of the self-occupied city formation, the early fault basin was transformed into a depression basin [63]. Although the compressional action of the late northern and southern orientations was based on the pretensioning structure, the cross-sectional tendency of the early extensional actions was not the same. According to the extension and extrusion critical surfaces as the inver-

sion interface, the fault inclines from the early extension northward to the later extension southward and forms an inverted fold structure in the shallow stratum. Figure 6(d) was modified according to the SB fault model established by Wang et al. [64], and the division of the Jh-K1sh fault zone in the upper part of the fault was added. As shown in Figure 6(b), only SYT2 contains a shallow seismic profile that can be used to estimate the velocity of the Quaternary to the surface seismic reflection layer and, in combination with Figure 6(d), the tectonic deformation in the study area. In Figure 6(e), the FNF zones can be observed in the black box, with a two-stroke travel time of 200–2000 ms for the effective exploration depth profile and an effective depth of 71–2392 m, determined by time-depth conversion. Propensity S of F3 and propensity N of fractures F1, F2, or F4 are

TABLE 3: Historical source information from Figure 4.

Sn	Date	Lat (°)	Lon (°)	Depth (°)	Ms	Source
1.	22 July 2017	45.25	124.69	12.1	4.9	Global CMT
2.	28 July 2017	45.26	124.73	14	3	
3.	4 Jan 2018	45.29	124.65	8	4.3	
4	5 March 2018	45.26	124.62	10	4.2	China Seismic Network
5.	23 April 2018	45.26	124.74	14	3.4	
6.	27 May 2018	45.24	124.64	10	5	
7.	27 May 2018	45.26	124.65	14.2	5.2	Global CMT
8.	28 May 2018	45.27	124.71	13	5.1	
9.	31 May 2018	45.23	124.64	7	3.6	
10.	31 May 2018	45.29	124.71	6	3.1	
11.	12 Aug 2018	45.24	124.67	9	3.2	
12.	15 Sept 2018	45.19	124.71	10	4.5	
13.	15 Sept 2018	45.29	124.66	10	4.4	China Seismic Network
14.	9 Nov 2018	45.26	124.75	8	2.6	
15.	30 Nov 2018	45.24	124.69	9	4	
16.	12 Jan 2019	45.24	124.65	9	3	
17.	11 May 2019	45.29	124.66	11	3.3	
18.	11 May 2019	45.27	124.74	10	2.6	
19.	17 May 2019	45.20	124.62	16.4	4.8	
20.	17 May 2019	45.24	124.68	14.2	5	Global CMT
21.	18 May 2019	45.30	124.75	10	5.1	
22.	19 July 2019	45.28	124.72	10	3.3	China Seismic Network
23.	26 Sept 2019	45.22	124.68	9	3.1	
24.	4 Oct 2019	45.23	124.69	9	2.8	

in the early stage of extensional fracture, the middle stage is in a relatively stable depression under extrusion, and the late stage is in pleated compressions.

The calculation of tectonic deformation was divided into three parts. First, we analyzed the process of the two fracture blocks to determine whether the changing trend was uplifted or subsided. Next, we assessed the changing thickness and formation age of the fractured strata. Finally, when the thickness of the formation was divided by the time of deposition or uplift, the result was structural deformation.

The black box of the Figure 6(b) seismic section in Figure 6(e) was enlarged, as shown in Figure 6(f). The fracture of F2 was first passed through the T02–T06 stratum to estimate the deformation of the upper and lower plate of the FNF. As shown in Figure 6(c), the average thickness of the upper plate was estimated to be 82.327 m, and the lower plate was 126.251 m, with a stratum age of 12.4 Ma. According to the formation thickness divided by formation age, formation structure deformation was obtained by 3.2 analysis of formation tectonic evolution, the upper plate tectonic deformation increased by 0.0966 mm/a, and the lower plate deformation subsidence decreased to 0.1047 mm. Such an extrapolation was used to estimate the uplift and settlement of the upper and lower plate, as presented in Table 5. Due to the lack of Quaternary borehole data, calibrating the shallow

seismic reflection layer was not possible, so the tectonic deformation was only estimated to be T02. The total structural deformation of the upper and lower plates estimated by SYT2 was taken as the average structural transformation in the study area.
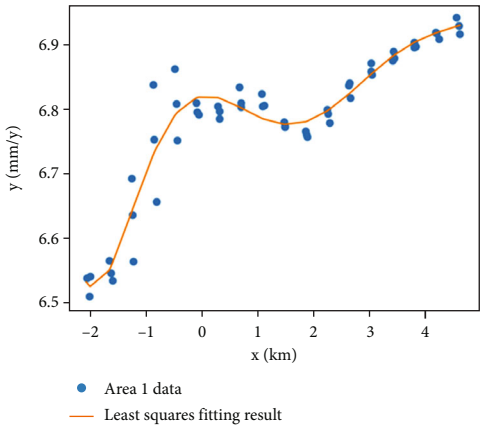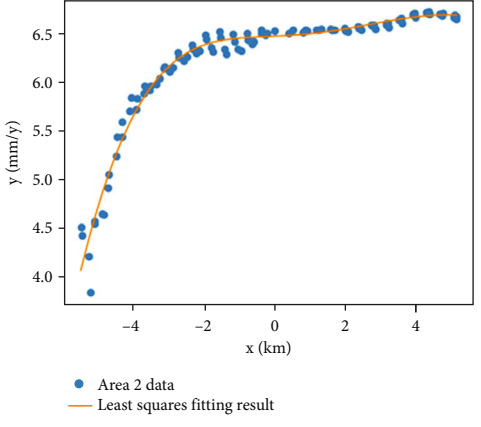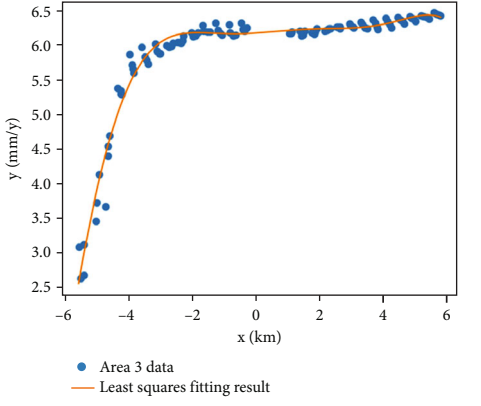
The calculation results are shown in Table 5. The upper plate of the FNF thrusts 0.2 mm/a upward relative to the lower plate, which is consistent with previous research results. The upper plate rises and the lower plate declines, which is an inverse fault.

5. GNSS and Plate Dynamics

The latest active age of the FNF is 23.9 ± 0.6 ka~28.9 ± 0.6 ka, making it a Late Pleistocene active fault [65]. A total of 26 shallow earthquakes occurred near the northern FNF zone from early 2017 to late 2019, with focal depths ranging from 6 to 14 km. The Ms 5.3 earthquake swarm occurred on 27 May 2018, and the magnitude was the highest so far. The Ms 5 earthquake swarm occurred on 18 May 2019, which made the SB the highest level II tectonic unit of seismic activity in Northeast China [66].

From Figures 6(a)–6(c), it can be seen that the two sections of the FNF are in the shape of letter "y," and the nature of the fault was dominated by normal faults in the early

TABLE 4: Fitting results of the polynomial least square method.

Fitting result	p	R^2 and RMSE (mm/a)
Area 1 data — Least squares fitting result	$P_1 = -51.8$ $P_2 = 142.4$ $P_3 = -120.9$ $P_4 = 22.97$ $P_5 = 13.56$ $P_6 = -4.663$ $P_7 = 0.147$ $P_8 = 6.818$	$R^2 = 0.9198$ RMSE = 0.0322
Area 2 data — Least squares fitting result	$P_1 = -3.768 \times 10^{-5}$ $P_2 = -1.259 \times 10^{-5}$ $P_3 = 1.772 \times 10^{-3}$ $P_4 = -1.05 \times 10^{-3}$ $P_5 = -1.596 \times 10^{-2}$ $P_6 = 2.302 \times 10^{-4}$ $P_7 = 0.087$ $P_8 = 6.467$	$R^2 = 0.9756$ RMSE = 0.09831
Area 3 data — Least squares fitting result	$P_1 = -17.666$ $P_2 = -1.845$ $P_3 = 24.467$ $P_4 = -7.31$ $P_5 = -3.11$ $P_6 = 1.01$ $P_7 = 0.208$ $P_8 = 6.145$	$R^2 = 0.9705$ RMSE = 0.1414

Cretaceous, which control the deposition of the northern faulted sag. The deposition thickness of the southern uplift is significantly smaller than that of the northern one, and the strong reflection layer is clear, continuous, and complete. It is inferred that the FNF was subjected to compression of the north-south direction in the late period, and its upper plate was thrust, and the surface was eroded and thinned. Since the neotectonic movement, the FNF has been characterized by thrusting, and the northern part has been transformed from a faulted sag (extension formed in fractured two blocks) to a depression (extrusion formed in fractured

two blocks). The depression boundary at the fault has been obviously dragged. The nature of the FNF thrust slip indicates that there is still compressive stress in the north-south direction, but it is not obvious in the east-west direction, and the horizontal stress can be seen from the GPS velocity field in Northeast China in Figure 4(c). The length of the red arrow indicates the size of the velocity. The length of the velocity in the legend is 5 mm/a. The red circle indicates the error ellipse. The smaller the circle, the more accurate the GPS velocity field; the overall direction of the GPS velocity field near the FNF is from west to east.
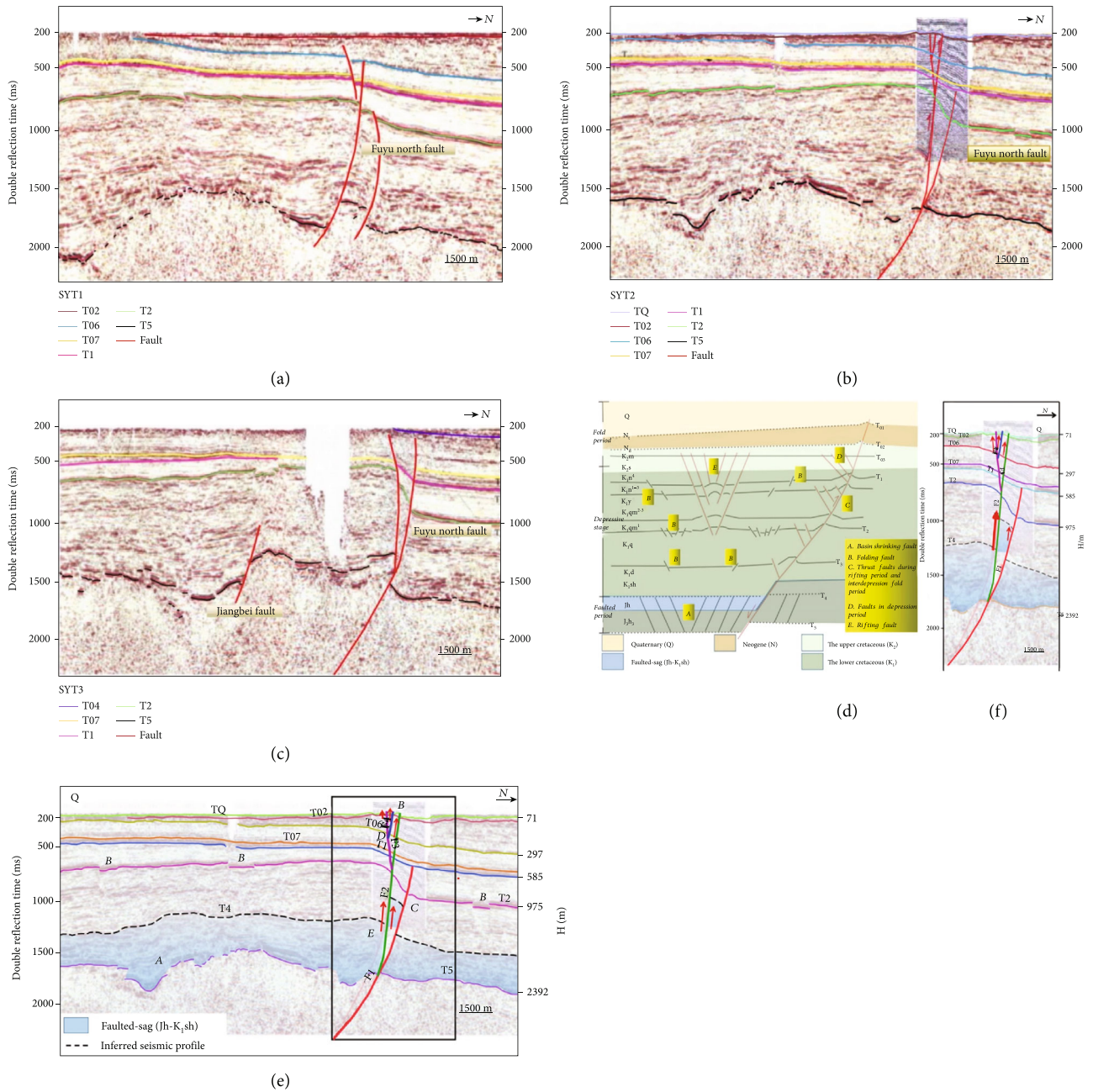
FIGURE 6: (a–c) The lower part of the FNF is faulted to the bedrock reflection layer, showing a normal fault layer. The fault in the upper strata is small, mainly showing the formation bending. The upper side of the FNF rises and the footwall falls, and the strata have a dragging phenomenon, owing to the reverse fault nature. (d) Regional tectonic stages and caprock fault system (modified by Wang et al. [64]). (e) Seismic reflection profiles of (b) and geological explanation. (f) The black box section in Figure 6(e). From the seismic reflection interfaces on the left side of F1, F2, F3, and F4, it can be seen that under the stress compression in the north-south direction, the upper plate of the FNF is uplifted by thrust, and the lower plate is decreased relative to the upper plate. The red arrow indicates the movement direction of the fault block under the compression of north-south stress.

The average velocity field on the SB is 2–8 mm/a, mainly in the east-west direction. There are 10–12 mm/a east-west and southeast velocity fields in the Japan Sea near the southeast of Heilongjiang Province in China.

The FNF in the study area is squeezed by five plates, namely, the Eurasian Plate in the northwest, the Siberia plate in the southwest, the Pacific Plate in the southeast, the Philippine Plate in the south, the Australian Plate, and the

Indian Ocean Plate in the northwest. The stress direction of the plates is shown in Figure 7. This direction is approximately perpendicular to the compressive stress trace, and this direction is close to the extrusion direction of the Eurasian Plate in the left coordinate system of Figure 7. In Figure 7, the 10–12 mm/a east-west and southeast-trending velocity fields in the Japanese Sea, which is on the southeast coast of Heilongjiang Province, China, may be related to the

Table 5: Results of uplift and subsidence of upper and lower reflectors in the SYT2 seismic profile.

Seismic reflection layer	Upper side (mm/a)	Footwall (mm/a)
T02–T06	+0.0066	−0.0102
T07–T06	+0.0161	−0.0161
T07–T1	+0.0179	−0.0179
T1–T2	+0.0112	−0.0240
T2–T4	+0.0139	−0.0159
T4–T5	+0.0309	−0.0206
Total	+0.0966	−0.1047

"mm/a" and "mm/yr" have the same meaning.

westward subduction of the Pacific Plate and the direction of the north-northeast advancement of the Philippine Plate, indicating that since the more recent tectonic movement has occurred, the north FNF has mainly experienced east-west and horizontal compression.

6. Discussion

6.1. Location Significance of the Study Area. The main faults in northeast China are NE and NW (Figure 4(c)). FNF, as a near EW fault in Late Pleistocene, is located at the intersection of NE and NW. The velocity field of FNF's north-facing GPS station changes from southeast to southeast, and the velocity field of FNF's south-facing GPS station changes from southeast to nearly east-west and then to southeast and east. Based on this change rule, we can first see that the Pacific Plate and Eurasian Plate move oppositely in the northwest (Figure 7). The change of the velocity field of the FNF northward GPS station is affected by the movement of the Siberian plate to the southwest and west. From the north to the south, the FNF northward is less and less affected by the Siberian plate, so the velocity field changes from southeast to southeast. In the south direction of FNF, the velocity field of the GPS station changes from southeast to near-east-west direction and then to southeast-east-east direction, influenced by the NWW movement of the Philippine Plate and Australian Plate. From this analysis, we can think that the position of FNF is the inflection point of tectonic plate dynamics in this region. It is of great significance to analyze the dynamics of surrounding plates with FNF as the research object.

6.2. Flower Structure. The vertical calculation results of the seismic reflection profile verified the results of the thrust on the hanging wall of the FNF. The quantitative calculation results showed that the vertical velocity of the FNF is 0.2 mm/a. These three seismic reflection profiles have a flower structure, which is the most typical sign of a fault strike-slip. In these structures, the main faults converge downward into the main displacement zone, and the upper dip angle of the fault becomes flat and flowery. When the strike-slip fault displacement is caused by compressive stress, there will be a "positive flower" structure (PFS), while the "negative flower" structure (NFS) is caused by tensile stress. The NFS was mainly in the lower part of the Upper

Cretaceous (T2–T11), indicating that it was in a tensile state. A normal flower structure mostly appeared in the late Upper Cretaceous (T07–T03), indicating that it was in a compressive stress state. In Figure 6(a), the NFS began to appear below the T2 layer, and the PFS appeared above it. In Figures 6(b) and 6(c), the PFS begins above T5, and there is no NFS feature below. These characteristics indicate that the image of compressive stress on the right side of SYT1 on the FNF is earlier than that on the left side, and the right side is not affected by tensile stress. The left side of SYT1 is at the edge of the FNF, and the extrusion effect was later than that on the right side, but it was greatly affected by early tensile stress. More regular flower structures cannot be found in Figures 6(a)–6(c), which may indicate that the strike-slip effect was not so strong, and the extrusion stress may be released in other ways.

6.3. Source of Strike-Slip Force on the Footwall of the FNF. The FNF intersects with the Second Songhua River Fault and with the NW strike, and its lower plate partially overlaps with the right plate of the Second Songhua River Fault. The lower plate of the FNF may have the same strike as the right plate of the Second Songhua River Fault. Zhang [69] believes that the northeast Yishu Fault and the Second Songhua River Fault are in maximum shear stress and have obvious conjugate structural activity characteristics and puts forward geological evidence of the left lateral of the Second Songhua River Fault, as shown in Figure 8.

Wang and Liu [70] discussed the evolution process of the Yitong-Shulan Fault, which experienced three stages and finally formed a right-lateral tensile shear fault. The network structure of the conjugate intersection of the Second Songhua River Fault and the Yitong-Shulan Fault conforms to the chessboard structure proposed by Li [71]. Based on this theory, the following change model is conceived, as shown in Figure 9. The location of each active fault is shown in Figure 4(d).

The chessboard structure model (Figure 9) combines the active faults involved in the study area into a grid that can be linked. In Figure 4(c), we can see that the velocity field near the FNF is mostly east-southeast and nearly horizontal. It shows that the force source in the east-west direction of the chessboard model is significantly greater than that in the north-south direction. In Figure 7, the main plate force source in the east-west direction of the FNF is the Eurasian Plate and the Pacific Plate. According to the vertical direction of the pink pressure line trajectory in Figure 7, the Australia plate, the Philippine plate, and the decomposition stress of the Eurasian Plate and Siberia plate in this vertical direction are relatively related, especially the Philippine Plate and Australia Plate. Although we have not been able to quantitatively analyze the contribution difference between the east-west- and north-south-related force source plates, we still obtained the following conclusions from the chessboard model (Figure 9). With the stress of the FNF near east-west under the extrusion of the Eurasian Plate and the Pacific Plate gradually increasing, the fractures F1 and F3 are similar to the scissors under the linkage of the chessboard model, and the upper is closed. The β angle gradually
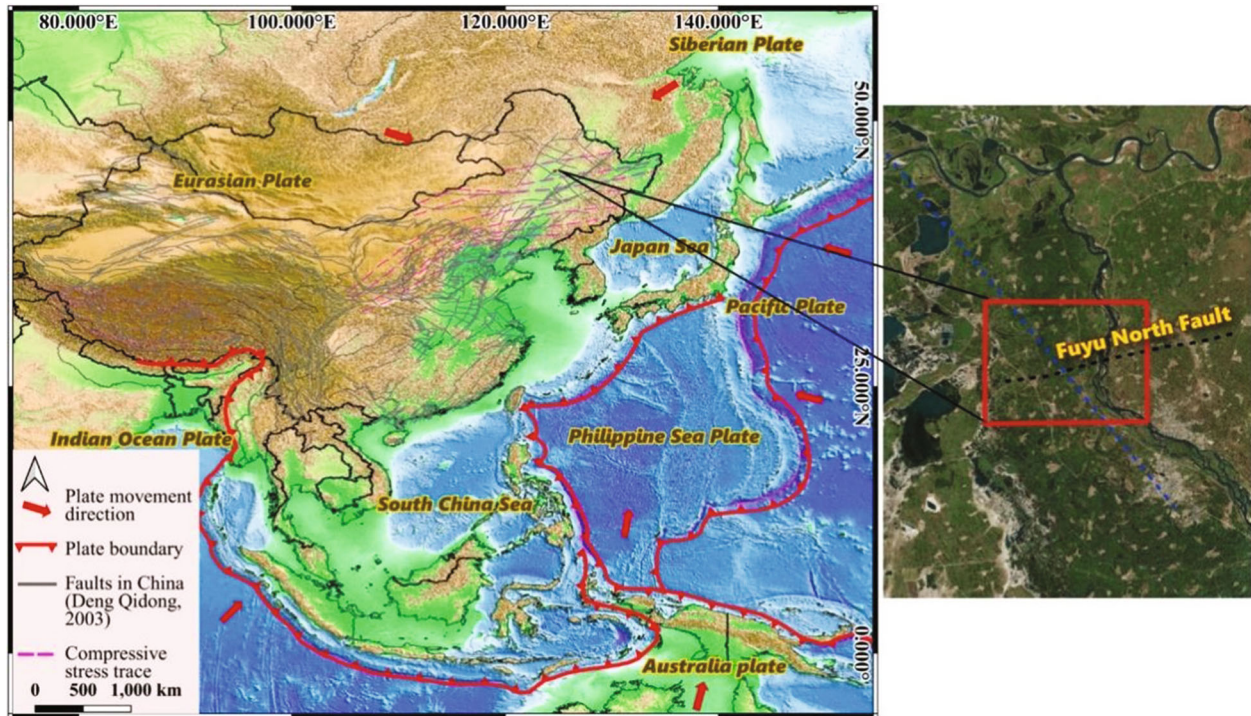
FIGURE 7: Spatial distribution of the East Asian continental marginal deformation system (plate boundary and direction [67], compressive stress trace [38], and fault in China [68]).

decreases, and the α angle gradually increases. The left side of F3 rises, the right side of F1 rises, and the left side occurs. The FNF is left-handed in the lower plate under the action of the Siberia plate, which makes the upper part of the intersection of the FNF, and the Second Songhua River Fault occurs as clockwise torsion. Section 2 obtained the left-handed result of the north fault by quantitative calculation, which can be reasonably explained by this model and previous evidence. Yu et al. [61] believed that the northward plate force of Australian and Philippine plates may be the reason for the formation of faulted sag or depressions in the SB. In Figure 1, the stress source in the faulted-sag area may be generated by the Eurasian Plate and the Pacific Plate in the extensional state, so the analysis of the source of force in the faulted-sag area may also involve the Australian Plate and the Philippine Plate.

6.4. Influence of Coulomb Stress. Table 2 lists the strongest seismic events in the three adjacent years near the FNF. Among them, the seismic event in 2018 was the largest magnitude in history. Only these three seismic events contain information on the focal mechanism. The focal mechanism is shown as strike-slip and is distributed at the bottom of the FNF. From Figure 6(b), it can be speculated that the FNF upper plate has mainly thrust faults and has strike-slip properties. The FNF thrust property was consistent with the results observed in Figures 6(a)–6(c). To answer whether the three earthquakes induce the reactivation of the surrounding surface faults, we can examine the induced effect of the three events on the surroundings by calculating the Coulomb stress.

We used the Coulomb 3.3 software provided by USGS to calculate the Coulomb stress. For the calculation process, we refer to Liu et al.'s [72] parameter; the crustal shear modulus is 3.3×10^4 MPa, Poisson's ratio is 0.25, and f' is 0.4 [73, 74]. Equation (9) is

$$\Delta \text{CFS} = \Delta \tau + f' \Delta \sigma_n. \tag{9}$$

$\Delta \tau$ represents the change of shear stress, $\Delta \sigma_n$ is the change of positive stress, and f' includes the characteristics of pore fluid and medium on the fault plane. The focal parameters of the three earthquakes are provided in Table 2. The dip thrust slip distance of the FNF is 0.2 mm, which is the calculation result of the three sections. Referring to the results of the two sections, the left-lateral slip distance of the FNF is 0.2 mm. The calculated results are shown in Figure 10.

Three earthquake events only induced part of the historical focal area; we can see that the Figure 10(a) event did not induce the Figure 10(b) event. However, the Figure 10(c) events were induced by the events in Figures 10(a) and 10(b). Combined with the analysis results of seismic profiles, we can see that these historical seismic events that were not induced were induced and unloaded in other ways.

6.5. Limitations. In the past, most of the research on fault activity is limited to the location of the study area, and most of them adopt several similar methods to deal with scientific problems through comparative analysis and mutual verification. The surrounding or larger scale plates may be closely related to it. This is different from the previous research
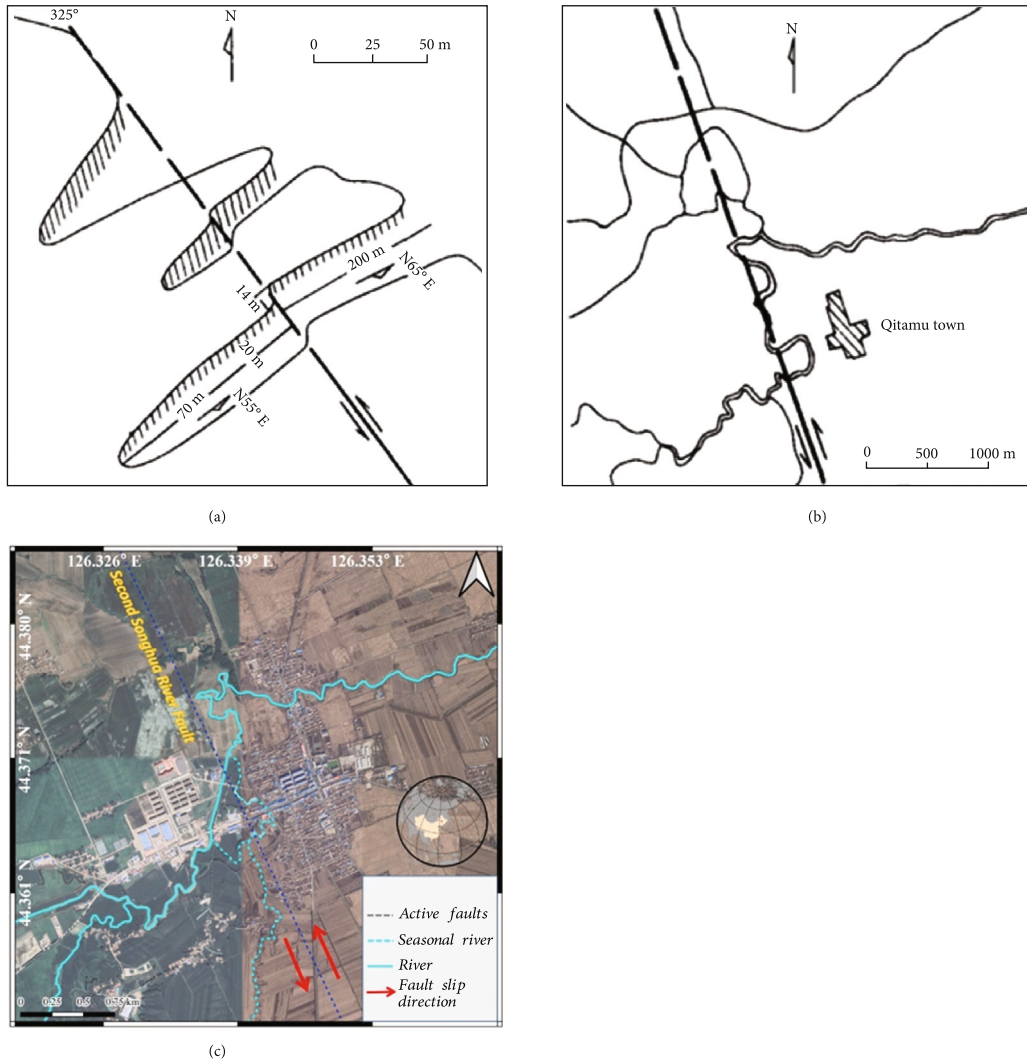
(a)

(b)

(c)

FIGURE 8: Second Songhua River left-handed geological evidence [69]. (a, b) The original image from Zhang [69]. (a) The schematic diagram of the slogan of the Sheling Liujia Village. (b) The intersection of the Second Songhua River tributary in Qitamu Town (Figures 1 and 3(c)). (c) The intersection of the Second Songhua River tributary in Google Maps; some rivers have dried up. They may turn into seasonal rivers, or this may be the impact of human factors on surface reconstruction. These do not affect the result of the left-handed fracture from the form of river dislocation bending. The exact location of (a) is not found in Google Maps, which may be because the surface has been converted into farmland.
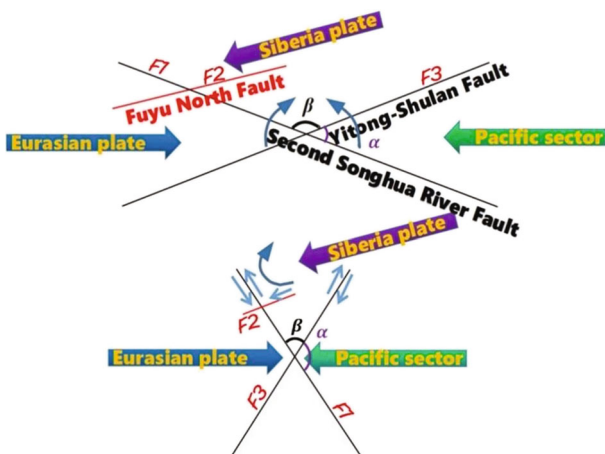

FIGURE 9: Chess format constructor.

ideas; in this paper, through the local extension to the surrounding fault, we analyze the activity of FNF from the perspective of larger-scale plate stress change. Multidisciplinary cross-analysis is used to fuse and reconstruct the data from geodetic technology including InSAR and GNSS using the VCE method. Seismic reflection profiles, structural models, and plate dynamics are analyzed from the perspective of structural geology and geophysics. Relying on the correlation of the overall analysis results, the relevant models are established based on the Li Siguang chessboard model, and relatively objective results are obtained. Although this is the innovation and advantages of this method, there are also some shortcomings. If the study area has Sentinel-1B of descending orbit and Sentinel-1B and Sentinel-1A of ascending orbit, the data after VCE fusion may be more accurate. This paper only
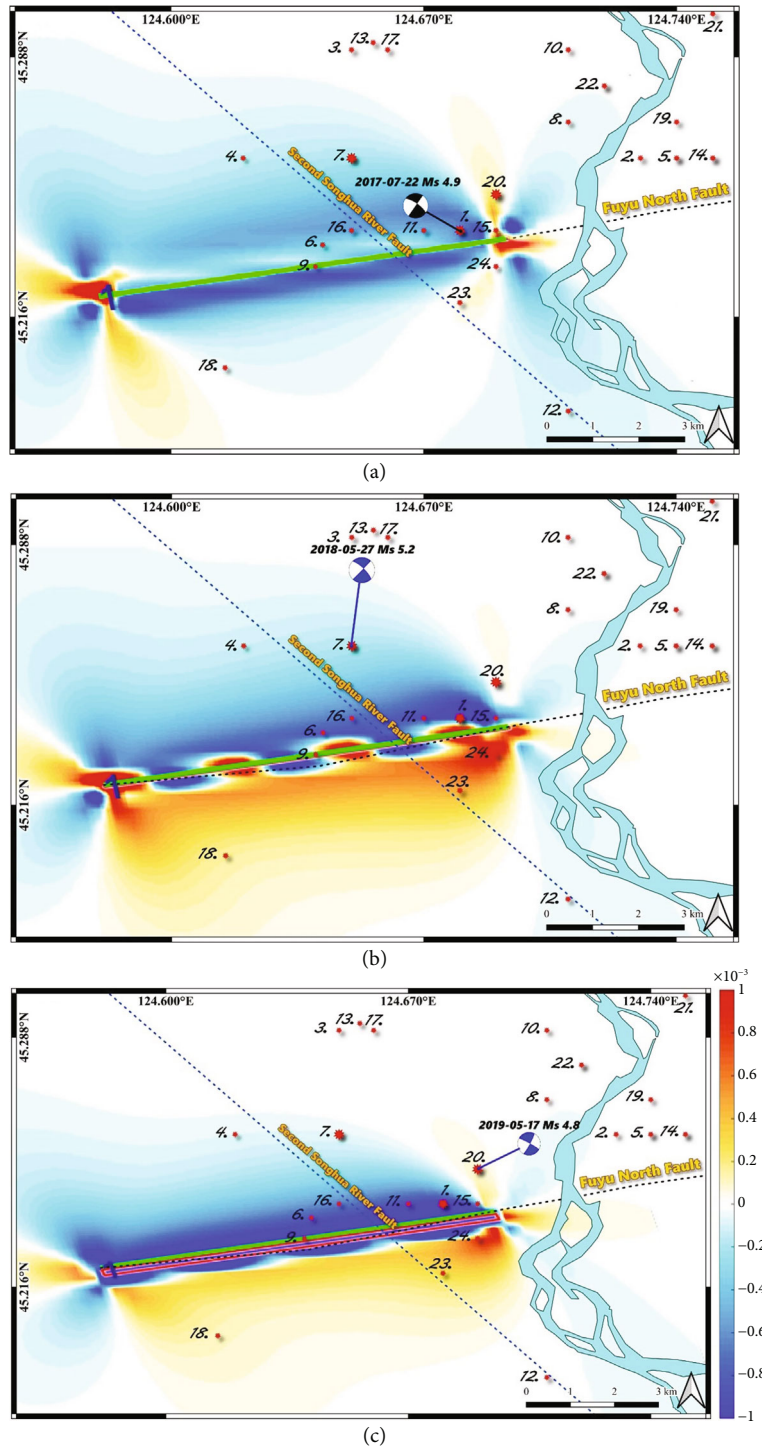
Figure 10: Coulomb stress (bar). The historical focal numbers of the three seismic events are the same (Figure 4 and Table 3). (a) The influence of seismic events on the surrounding stress is mainly unloading, and the loading-induced positions are serial numbers 15, 20, 23, and 24. (b) The unloading area is mainly distributed in the lower plate of the FNF, and the loading area is mainly distributed in the upper plate of the FNF and the fault. Compared with (a), the magnitude is larger, and the loading value at both ends of the seismogenic fault is larger. The loading-induced positions are serial numbers 1, 9, 18, 20, 23, and 24. (c) The distribution of the unloading area is similar to that of (b), but the value is slightly smaller. The loading-induced locations are serial numbers 18, 20, 23, and 24.

shows the stress field of GPS stations in Northeast China, and the surrounding plate is analyzed by previous results. If the GPS stress field of the surrounding plate can be independently calculated, it may be able to calculate the change of the surrounding plate more accurately and quantitatively.

7. Conclusions

In this study, we use the time-series Sentinel-1B descending orbit data to calculate the east-west results and GPS east-west data, using VCE fusion reconstruction, so that the reconstructed data not only has the characteristics of large density of InSAR data but also has the characteristics of high accuracy of GPS in the horizontal. The polynomial least square method is used to fit the three east-west point data. The distribution of the east-west velocity field near FNF is studied, and the conclusion of FNF left-handed is obtained. The subsidence velocity of FNF underground structure is quantitatively estimated using the SYT2 seismic profile. The thrust velocity of 0.2 mm/a indicates that the vertical velocity of FNF is slow. The horizontal velocity of GNSS stations near FNF has certain regularity, revealing that the region where FNF is located is the inflection point of the horizontal velocity field change in Northeast China. Referring to the previous three horizontal sliding evidences of the Yitong-Shulan Fault and the Second Songhuajiang Fault, we qualitatively analyze the possible change factors and process of FNF fault in the past and present based on the Li Siguang chessboard model and the dynamic change characteristics of surrounding plates. Our results show that the compressive stress in the north-south direction gradually decreases and the compressive stress in the east-west direction gradually increases.

In future research, we can start from the perspective of the microscopic microstructure and combine the method of rock dating to quantitatively analyze the stress of each fracture and deduce the temporal variation of the fractures. This will combine qualitative and quantitative analysis and macro- and microanalysis of fracture activity; such geological evidence tends to be objective.

Data Availability

Both Tables 2 and 3 are from the Global CMT website. Details of GNSS results can be obtained by sending an email request to author Bin Liu.

Conflicts of Interest

No conflicts of interest exist.

Acknowledgments

References

[1] International Atomic Energy Agency, "Site Evaluation for Nuclear Installations," in *IAEA Safety Standards Series No. SSR-1*, IAEA, Vienna, Austria, 2019.

[2] T. Maruyama, "Paleoseismological evidence for non-characteristic behavior of surface rupture associated with the 2007 Mid-Niigata Prefecture earthquake, Central Japan," *Tectonophysics*, vol. 429, pp. 45–60, 2007.

[3] T. Nishimura, M. Tobita, H. Yarai et al., "Episodic growth of fault-related fold in northern Japan observed by SAR interferometry," *Geophysical Research Letters*, vol. 35, no. 13, 2008.

[4] Z. H. Wu, "The definition and classification of active faults: history, current status and progress," *Acta Geoscientica Sinica*, vol. 40, pp. 661–697, 2019.

[5] L. Y. Fu, "A preliminary study on historical earthquakes in Northeast China," *Journal of Northeast Normal University (Natural Science Edition)*, vol. 2, pp. 166–173, 2015.

[6] Y. D. Quan, "Further research on characteristics of the seismic activity in northeast China area," *Earthquake*, vol. 5, pp. 52–55, 2018.

[7] C. Y. Li, Y. P. Wang, and J. Shen, "Discussion on new activity of the second Songhuajiang fault," *Seismology and Geology*, vol. 21, no. 4, pp. 351–361, 1999.

[8] W. Z. Fu and R. Z. He, "Structural characteristics of earthquakes in Songliao Basin and its peripheral regions," *World Geology*, vol. 18, pp. 95–101, 1999.

[9] L. X. Gao and Y. Dai, "The present geodynamic environment of Northeast China," *Journal of Geodesy and Geodynamics*, vol. 40, pp. 1101–1107, 2020.

[10] H. Z. Zhu, "Ground collapse and earthquake damage," *Soil and Water Conservation in China*, vol. 5, pp. 18-19, 1988.

[11] X. H. Liang, B. Jiang, J. C. Dong, and S. H. Liu, "Risk evaluation of surface dislocation caused by earthquake," *Seismology and Geology*, vol. 24, no. 4, pp. 495–502, 2002.

[12] B. Wan, C. B. Gao, and S. C. Zheng, "Features and circumstances for surface seismic ruptures," *Seismological Research of Northeast China*, vol. 20, no. 1, pp. 1–8, 2004.

[13] B. Shao, J. Shen, X. H. Yu, and X. Y. Dai, "Study on the uncoordinated mechanism between surface deformation scale of buried active faults and source scale," *Geological Review*, vol. 61, pp. 699-700, 2015.

[14] J. Y. Han, N. J. Huang, and J. T. Y. Chuang, "Application of laser scanning for rapid geologic documentation of trench exposures," *Engineering Geology*, vol. 224, pp. 97–104, 2017.

[15] T. Shiki, M. B. Cita, and D. S. Gorsline, "Sedimentary features of seismites, seismo-turbidites and tsunamiites–an introduction," *Sedimentary Geology*, vol. 135, no. 1-4, pp. vii–ix, 2000.

[16] C. Montenat, P. Barrier, and d.' E. P. Ott, "Seismites: an attempt at critical analysis and classification," *Sedimentary Geology*, vol. 196, no. 1-4, pp. 5–30, 2007.

[17] M. Pisarska-Jamroży, S. Belzyt, A. Börner et al., "Evidence from seismites for glacio-isostatically induced crustal faulting in front of an advancing land-ice mass (Rügen Island, SW Baltic Sea)," *Tectonophysics*, vol. 745, no. 1, pp. 338–348, 2018.

[18] L. Stamatopoulos, E. Kamberis, and G. Alevizos, "Detection of active fault scarps in Western Peloponnese, Greece," *Quaternary International*, vol. 508, pp. 88–97, 2019.

[19] R. E. Wallace, "Profiles and ages of young fault scarps, north-central Nevada," *Geological Society of America Bulletin*, vol. 88, no. 9, pp. 1267–1281, 1977.

[20] M. Meghraoui, H. Philip, F. Albarede, and A. Cisternas, "Trench investigations through the trace of the 1980 EI Asnam thrust fault: evidence for paleoseismicity," *Bulletin of the Seismological Society of America*, vol. 78, no. 2, pp. 979–999, 1988.

[21] F. H. Swan, "Temporal clustering of paleoseismic events on the Oued Fodda fault, Algeria," *Geology*, vol. 16, no. 12, pp. 1092–1095, 1988.

[22] H. Philip, E. Rogozhin, A. Cisternas, J. C. Bousquet, B. Borisov, and A. Karakhanian, "The Armenian earthquake of 1988 December 7: faulting and folding, neotectonics and palaeoseismicity," *Geophysical Journal International*, vol. 110, no. 1, pp. 141–158, 1992.

[23] R. S. Yeats, K. Sieh, and C. R. Allen, *The Geology of Earthquakes*, Oxford University Press, Oxford, USA, 1997.

[24] Z. Y. Yu, N. Yin, C. Y. Wang, M. Deng, and W. G. Lan, "Active tectonics, paleoseismology and seismic hazards of the piedmont Xizhoushan fault zone in the Shanxi graben system, North China Block," *Journal of Asian Earth Sciences*, vol. 205, article 104590, 2021.

[25] P. Molnar, E. T. Brown, B. C. Burchfiel et al., "Quaternary climate change and the formation of river terraces across growing anticlines on the north flank of the Tien Shan, China," *The Journal of Geology*, vol. 102, no. 5, pp. 583–602, 1994.

[26] G. E. Campbell, R. T. Walker, K. Abdrakhmatov et al., "The Dzhungarian fault: late quaternary tectonics and slip rate of a major right-lateral strike-slip fault in the northern Tien Shan region," *Journal of Geophysical Research*, vol. 118, no. 10, pp. 5681–5698, 2013.

[27] T. Rockwell, E. Keller, and G. Dembroff, "Quaternary rate of folding of the Ventura Avenue anticline, western transverse ranges, Southern California," *Geological Society of America Bulletin*, vol. 100, no. 6, pp. 850–858, 1988.

[28] Y. Yao, J. Chen, T. Li et al., "Soil liquefaction in seasonally frozen ground during the 2016 Mw6.6 Akto earthquake," *Soil Dynamics and Earthquake Engineering*, vol. 117, pp. 138–148, 2019.

[29] K. O. Cetin, R. B. Seed, R. E. Kayen et al., "Examination of differences between three SPT-based seismic soil liquefaction triggering relationships," *Soil Dynamics and Earthquake Engineering*, vol. 113, pp. 75–86, 2018.

[30] L. G. Oka, M. Dewoolkar, and S. M. Olson, "Comparing laboratory-based liquefaction resistance of a sand with non-plastic fines with shear wave velocity-based field case histories," *Soil Dynamics and Earthquake Engineering*, vol. 113, pp. 162–173, 2018.

[31] R. S. Olsen, "Liquefaction analysis using the cone penetrometer test," in *Proceedings of the 8th World Conference on Earthquake Engineering*, San Francisco, 1984, Earthquake Engineering Research Institute, USA.

[32] P. Zhang, D. F. Zhang, Y. Yang et al., "A case study on integrated modeling of spatial information of a complex geological body," *Lithosphere*, vol. 2022, no. Special 10, p. 2918401, 2022.

[33] X. Li, Q. Li, Y. Hu et al., "Study on three-dimensional dynamic stability of open-pit high slope under blasting vibration," *Lithosphere*, vol. 2022, no. Special 4, article 6426550, 2022.

[34] Z. Dou, S. X. Tang, X. Y. Zhang et al., "Influence of shear displacement on fluid flow and solute transport in a 3D rough fracture," *Lithosphere*, vol. 2021, no. Special 4, p. 1569736, 2021.

[35] D. Chen, H. Chen, W. Zhang, J. Lou, and B. Shan, "An analytical solution of equivalent elastic modulus considering confining stress and its variables sensitivity analysis for fractured rock masses," *Journal of Rock Mechanics and Geotechnical Engineering*, vol. 14, pp. 825–836, 2022.

[36] Z. Dou, Y. M. Liu, X. Y. Zhang et al., "Influence of layer transition zone on rainfall-induced instability of multilayered slope," *Lithosphere*, vol. 2021, no. Special 4, article 2277284, 2021.

[37] G. Li, Y. Hu, and T. Sm, "Analysis of deformation control mechanism of prestressed anchor on jointed soft rock in large cross-section tunnel," *Bulletin of Engineering Geology and the Environment*, vol. 80, no. 12, pp. 9089–9103, 2021.

[38] J. Shen and J. Bo, *Exploration of Active Faults and Evaluation of Seismic Hazard in Sonyuan City*, Seismological Press, Beijing, China, 2016.

[39] J. C. Zhu, Y. L. Feng, Q. R. Meng, S. H. Li, J. L. Wu, and R. X. Zhu, "Decoding stratigraphic and structural evolution of the Songliao Basin: implications for late Mesozoic tectonics in NE China," *Journal of Asian Earth Sciences*, vol. 194, article 104138, 2020.

[40] A. Hooper, "A multi-temporal InSAR method incorporating both persistent scatterer and small baseline approaches," *Geophysical Research Letters*, vol. 35, no. 16, p. L16302, 2008.

[41] P. Berardino, G. Fornaro, R. Lanari, and E. Sansosti, "A new algorithm for surface deformation monitoring based on small baseline differential SAR interferograms," *IEEE Transactions on Geoscience and Remote Sensing*, vol. 40, no. 11, pp. 2375–2383, 2002.

[42] E. A. Hetland, P. Musé, M. Simons, Y. N. Lin, P. S. Agram, and C. J. DiCaprio, "Multiscale InSAR time series (MInTS) analysis of surface deformation," *Journal of Geophysical Research*, vol. 117, no. B2, article B02404, 2012.

[43] G. Liu, X. Ding, Y. Chen, Z. L. Li, and D. W. Zheng, "New and potential technology for observation of earth from space: synthetic aperture radar interferometry," *Advances in Earth Science*, vol. 15, no. 6, pp. 734–740, 2000.

[44] D. Massonnet, M. Rossi, C. Carmona et al., "The displacement field of the Landers earthquake mapped by radar interferometry," *Nature*, vol. 364, no. 6433, pp. 138–142, 1993.

[45] A. Ferretti, C. Prati, and F. Rocca, "Nonlinear subsidence rate estimation using permanent scatterers in differential SAR interferometry," *IEEE Transactions on Geoscience and Remote Sensing*, vol. 38, no. 5, pp. 2202–2212, 2000.

[46] T. J. Wright, B. E. Parsons, and Z. Lu, "Toward mapping surface deformation in three dimensions using InSAR," *Geophysical Research Letters*, vol. 31, no. 1, 2004.

[47] J. Hu, Z. W. Li, X. L. Ding, and J. J. Zhu, "Two-dimensional coseismic surface displacements field of the Chi-Chi earthquake inferred from SAR image matching," *Sensors*, vol. 8, no. 10, pp. 6484–6495, 2008.

[48] J. Hu, Z. W. Li, J. J. Zhu, and X. L. Ding, "Three-dimensional surface displacements from InSAR and GPS measurements with variance component estimation," *IEEE Geoscience and Remote Sensing Letters*, vol. 9, no. 4, pp. 754–758, 2012.

[49] J. D. Gergonne, "The application of the method of least squares to the interpolation of sequences," *Historia Mathematica*, vol. 1, no. 4, pp. 439–447, 1974.

[50] S. M. Gergonne, "Paper on the design and analysis of polynomial regression experiments," *Historia Mathematica*, vol. 1974, no. 1, pp. 431–439, 1974.

[51] D. Q. Xing, Y. J. Liu, Z. X. Tang et al., "Research on upper Paleozoic tectonic framework and evolution of Songliao Basin," *Global Geology*, vol. 34, pp. 396–407, 2015.

[52] G. Q. Ma and Q. F. Meng, "Structure identification by gravity anomaly in Songliao Basin," *Journal of Jilin University*, vol. 48, no. 2, pp. 507–516, 2018.

[53] W. Guo, Z. J. Liu, H. M. Dong, and Y. J. Zhao, "The sequence stratigraphic features and hydrocarbon accumulation of Songliao Basin," *Journal of Jilin University*, vol. 34, no. 2, pp. 216–221, 2004.

[54] H. B. Jia, H. C. Ji, L. W. Wang, D. J. Yang, P. W. Men, and C. Shi, "Tectono-sedimentary and hydrocarbon potential analysis of rift-related successions in the Dehui depression, Songliao Basin, northeastern China," *Petroleum Geology*, vol. 76, pp. 262–278, 2016.

[55] S. Mizutani, J. A. Shao, and Q. L. Zhang, "The Nadanhada terrane in relation to mesozoic tectonics on continental margins of East Asia," *Acta Geologica Sinica*, vol. 3, pp. 204–216, 1989.

[56] Y. P. Zhang, W. M. Song, F. C. Na, Q. Z. Bao, and Y. Wang, "Characteristics of the tectonic framework of northeast Asian mesozoic active continental margin," *Geology and Resources*, vol. 25, no. 5, pp. 407–422, 2016.

[57] P. J. Wang, F. Mattern, A. N. Didenko, D. F. Zhu, B. Singer, and X. M. Sun, "Tectonics and cycle system of the Cretaceous Songliao Basin: an inverted active continental margin basin," *Earth-Science Reviews*, vol. 159, pp. 82–102, 2016.

[58] C. Y. Chen, *Volcanostratigraphic Sequence and Tectonic-Volcanic-Basin Filling Evolution in the Faulted Period of Songliao Basin–Based on the Comparative Study of Basin Margin Sections and Xujiaweizi Graben, [Ph.D. thesis]*, Jilin University, China, 2016.

[59] W. U. Zhao, C. Zou, Z. Feng et al., "Geological features and evaluation techniques of deep-seated volcanics gas reservoirs, Songliao Basin," *Petroleum exploration and development*, vol. 35, no. 2, pp. 129–142, 2008.

[60] S. Z. Sheng, Y. G. Wan, X. S. Wang, J. C. Huang, Z. G. Xu, and J. Li, "Relocation of the 2013 Songyuan earthquake swarm in Jilin province and its seismogenic structure," *Earth Science Frontiers*, vol. 24, no. 2, pp. 212–219, 2017.

[61] C. Yu, N. T. Penna, and Z. H. Li, "Generation of real-time mode high-resolution water vapor fields from GPS observations," *Journal of Geophysical Research*, vol. 122, no. 3, pp. 2008–2025, 2017.

[62] C. Yu and Z. H. Li, "Interferometric synthetic aperture radar atmospheric correction using a GPS-based iterative tropospheric decomposition model," *Remote Sensing of Environment*, vol. 204, pp. 109–121, 2018.

[63] Z. Liu, J. Song, X. Liu, X. Wu, and X. Gao, "Discovery of the Cretaceous-Paleogene compressional structure and basin properties of the southern Songliao Basin," *Acta Petrologica Sinica*, vol. 36, no. 8, pp. 2383–2393, 2020.

[64] Y. C. Wang, Z. L. Huang, and B. Z. Liu, "The petroleum system in the south of Songliao Basin," *Petroleum Exploration and Development*, vol. 28, pp. 16–20, 2001.

[65] Y. K. Wan, J. Shen, X. Liu et al., "The discovery and identification of activities of the Fuyu North Fault in Songyuan," *Earthquake Research in China*, vol. 32, pp. 477–484, 2016.

[66] E. Z. Li, C. Liu, L. H. Zhang, and Z. F. Zeng, "The correlation of structure and earthquake in Songliao Basin," *Progress in Geophysics*, vol. 27, pp. 1337–1349, 2012.

[67] J. T. Li, J. Zhang, and L. J. F. Major, "Deformation Systems in Mainland China," *The Frontier of Earth Science (China University of Geosciences (Beijing): Peking University)*, vol. 21, no. 3, pp. 226–245, 2014.

[68] Q. D. Deng, L. C. Chen, and Y. K. Ran, "Quantitative studies and applications of active tectonics," *Earth Science Frontiers*, vol. 11, no. 4, pp. 383–392, 2004.

[69] Z. Q. Zhang, "The characterstics of the Songhuajiang Fault activity and preliminary discussion on the cause of seismicity in the Yitong-Shulan Fault," *Seismological Research of Northeast China*, vol. 3, pp. 73–80, 1987.

[70] C. J. Wang and S. P. Liu, "Evolution of the Yitong-Shulan Fault zone and modelling on earthquake risk district," *Journal of Jilin Unviersity (Earth Science Edition)*, vol. 17, pp. 21–29, 1987.

[71] S. G. Li, *Introduction to Geomechanics*, Science Press, Beijing, China, 1969.

[72] H. Liu, Y. Ba, and B. Liu, "The influence study of static coulomb stress change generated in Qianguo Ms 5.8 earthquake of Jilin Province in 2013," *Journal of disaster prevention and reduction*, vol. 30, no. 3, pp. 16–19, 2014.

[73] G. C. P. King, R. S. Stein, and J. Lin, "Static stress changes and the triggering of earthquakes," *Bulletin of the Seismological Society of America*, vol. 84, no. 3, pp. 935–953, 1994.

[74] T. Parsons, C. Ji, and E. Kirby, "Stress changes from the 2008 Wenchuan earthquake and increased hazard in the Sichuan Basin," *Nature*, vol. 454, no. 7203, pp. 509-510, 2008.